photonics

Article

Simulated LCSLM with Inducible Diffractive Theory to Display Super-Gaussian Arrays Applying the Transport-of-Intensity Equation

Jesus Arriaga-Hernandez [1,*], Bolivia Cuevas-Otahola [2,*], Jacobo Oliveros-Oliveros [1], María Morín-Castillo [3], Ygnacio Martínez-Laguna [4] and Lilia Cedillo-Ramírez [4]

1 Facultad de Ciencias Físico Matemáticas (FCFM), Benemérita Universidad Autónoma de Puebla (BUAP), Av. San Claudio y 18 Sur, Col. San Manuel, Puebla C.P. 72570, PUE, Mexico
2 Instituto de Radioastronomía y Astrofísica (IRyA), Universidad Nacional Autónoma de México (UNAM), Antigua Carretera a Pátzcuaro, Morelia C.P. 58089, MICH, Mexico
3 Facultad de Ciencias de la Electrónica (FCE), BUAP, Av. San Claudio y 18 Sur, Col. San Manuel, Puebla C.P. 72570, PUE, Mexico
4 Instituto de Ciencias de la Universidad Autónoma de Puebla (ICUAP), BUAP, IC 10 San Claudio Av. Cd Universitaria, Jardines de San Manuel, Puebla C.P. 72572, PUE, Mexico
* Correspondence: jesus.arriagahdz@correo.buap.mx (J.A.-H.); b.cuevas@irya.unam.mx (B.C.-O.)

Abstract: We simulate a liquid crystal spatial light modulator (LCSLM), previously validated by Fraunhofer diffraction to observe super-Gaussian periodic profiles and analyze the wavefront of optical surfaces applying the transport-of-intensity equation (TIE). The LCSLM represents an alternative to the Ronchi Rulings, allowing to avoid all the related issues regarding diffractive and refractive properties, and noise. To this aim, we developed and numerically simulated a LCSLM resembling a fractal from a generating base. Such a base is constituted by an active square (values equal to one) and surrounded by eight switched-off pixels (zero-valued). We replicate the base in order to form $1 \times N$-pixels and the successive rows to build the 1024×1024 LCSLM of active pixels. We visually test the LCSLM with calibration images as a diffractive object that is mathematically inducible, using mathematical induction over the $N \times N$-shape ($1 \times 1, 2 \times 2, 3 \times 3, \ldots, n \times n$ pixels for the generalization). Finally, we experimentally generate periodic super-Gaussian profiles to be visualized in the LCSLM (transmission SLM, 1024×768-pixels LC 2012 Translucent SLM), modifying the TIE as an optical test in order to analyze the optical elements by comparing the results with ZYGO/APEX.

Keywords: super-Gaussian patterns; inducible patterns; irradiance transport equation; Fraunhofer diffraction; patterns in geometric series; wavefront sensing

check for updates

Citation: Arriaga-Hernández, J.; Cuevas-Otahola, B.; Oliveros-Oliveros, J.; Morín-Castillo, M.; Martínez-Laguna, Y.; Cedillo-Ramírez, L. Simulated LCSLM with Inducible Diffractive Theory to Display Super-Gaussian Arrays Applying the Transport-of-Intensity Equation. *Photonics* **2023**, *10*, 39. https://doi.org/10.3390/photonics10010039

Received: 23 November 2022
Revised: 20 December 2022
Accepted: 21 December 2022
Published: 30 December 2022

1. Introduction

Nowadays, spatial light modulators (SLMs) [1] are of significant relevance in the development of several techniques and applications, namely, in diverse sciences, medicine [2–6], lithography [7], quantum optics [8], optical trapping [9], etc., being holography among the disciplines where SLM are more widely used along with diffractive and interferometric elements [10,11]. In the literature, it is possible to find a significant number of SLM, as in the liquid crystal displays (LCDs), the twist nematic-LCD (TNLCD), nematic and smectic thermotropic SLM, parallel-aligned nematic-liquid-crystal SLM (PAL-SLM), etc. [1,10,12]. Hence, the SLM is an optoelectronic instrument [1,10,11] that provides multiple benefits, allowing to generate and observe a large number of patterns on a surface, as well as controlling certain states of polarization [11,13], considering the resolution and manufacturing process [1,10]. Moreover, the SLM diffractive properties have been studied, for example, in the work by Davis et al. [14], where in addition, the transmission and refractive properties of the LCSLM (liquid crystal SLM) have been addressed, or in the work by

Pérez-Cabré et al. [15], where they study high-order diffractive processes using diverse elements and an LCoS-SLM (liquid crystal on silicon). In this work, we consider diffractive Fraunhofer phenomena and we address them as in previous works by Katz et al. [16] and Agour et al. [17] in order to analyze the effects in the SLM. Considering the previous arguments related to the SLM in this work, as a first step, we build an algorithm to simulate an LCSLM (LCD in the following) without considering its chemistry or all the polarization elements inherent to the arrays involving the SLM [1,10–12,14–17]. We build the LCD resembling a fractal [18–20] from a base constituted by a square with a transmission equal to 1 surrounded by 0-transmission squares. Subsequently, we validated the LCD from its diffractive properties (following a prescription similar to that in the work by Agour [17] and Pérez-Cabré et al. [15]), proposing a high-order diffractive process mathematically inducible [21], to validate the resolution of the $N \times N$ simulated LCD. As a third step, we built super-Gaussian (SG) periodic patterns to visualize them in the LCD. Subsequently, we generate the SG pattern in the LCD to use them in the transport-of-intensity equation (TIE) to test optical elements, solving it as a differential equation to obtain the wavefront $W(x, y)$ [22,23]. Finally, we consider $W(x, y)$ in terms of the Zernike aberrations polynomial [24–26] to compare our results with ZYGO/APEX (as a combination between ZYGO [27] and APEX), and also with the conventional TIE [23,28] for three optical elements (L1, L2, and L3). Furthermore, we created a repository (Matlab codes repository https://github.com/umbramortem/SG_profile_LCLSM_inductible_diffractive, accessed on 24 December 2022) containing all the software tools used to build the simulations and obtain the results along with the images required to execute the tools using the Zernike coefficients. The repository sections follow the structure of this paper. We include as well Supplementary Materials, with all the calculations to show that the simulated LCSLM represents a mathematically inducible diffractive object.

2. LCD Design and Construction

In order to design the LCD, we did not simulate the polarization effects since, numerically speaking, the wavefront can be built and visualized straightforwardly. We stress the previous argument given that often the polarizer is placed before and after the LC-SLM [15,17]. We recall that fractals are generated from a base, subsequently multiplied, added, or joined in specific points, as required, given the desired fractal features (auto similarity) [18–20]. The base (constructed in Section I in the code LCD_LCSLM_DiffPattern_SGR.m in the repository) is constituted by nine squares, eight black ones surrounding a white square (square-shaped window) [29]. Such a base represents the active value of our simulated LCD (Figure S1a in Supplementary Materials), considering that the base squares are pixels or array entries, in Matlab®, in the particular case of this work. The latter implies that the minimum value for an entry or pixel should be 1 (considering a square matrix), avoiding problems with the Whittaker–Nyquist–Kotelnikov–Shannon sampling theorem (Nyquist theorem) [30–32]. We consider the base and integrate more elements to it, with the same features on the right side, up to a $1 \times N$-size pixels array (according to Supplementary Materials), in order to generate all the LCD pixels (as in Section II in the code LCD_LCSLM_DiffPattern_SGR.m). Subsequently, we replicate row $1 \times N$, N times, placing each replica immediately below the previous one, with each constituting pixel abiding by the base and order of the 0 and 1 squares, resulting in our $N \times N$-pixels LCD, built from the base (Figure S1a in Supplementary Materials), resembling a fractal [18–20].

LCD Validation

In order to validate the simulated LCD, we consider its construction process and Fraunhofer diffraction [33–35], such as the diffraction patterns simulating the LCDs, constituting an inducible process [21] (we include the detailed calculations as Supplementary Materials). We consider the diffractive field $U(x, y)$ from the following expression:

$$U(x,y) = \frac{e^{ikz}}{ikz} e^{i\frac{k}{2z}\left(x^2+y^2\right)} \iint_{-\infty}^{\infty} \widetilde{U_0}(\xi,\eta) e^{-i\frac{2\pi}{z\lambda}(x\xi+y\eta)} d\xi d\eta, \tag{1}$$

with $\widetilde{U_0}(\xi,\eta)$ representing the diffractive object considering the wavelength λ (HeNe laser with $\lambda = 632$ nm), where z is the distance between the LCD ($z = 100$ mm, Figure S1a in Supplementary Materials) [33–35]. Experimentally, we consider the LCD case with side $a = 36$ µm (LCSLM transmissive HOLOEYE LC 2012), modeled by $\mathrm{rect}(\xi/a)$ functions, and the intensity value given by the square modulus function $I(x,y) = |U(x,y)|^2$. Moreover, we obtain the Fraunhofer diffraction by recalling the required relation, where $z > 2\frac{a^2}{\lambda}$ [33–35], for which it holds $z = 0.004$ m and $2\frac{a^2}{\lambda} = 114$ µm. We notice a certain series expansion in the terms $S_{a,b}(x)$ and $S_{a,b}(y)$. The latter implies that the diffraction field in an LCD with identical, periodical equidistant pixels follows a certain expansion pattern regarding the number of pixels. Such a series expansion is the so-called geometric series [36–38], widely used for real and complex numbers. This series has several salient features, among which stands out its capability to be reduced to a ratio involving $(N+1)$-th terms and the first one (with its convergence depending on the limiting value of the N-th term). Moreover, the geometric series is inducible [21]; hence, it is straightforward (from a significant number of calculations) to test that $U_{N\times N}$ is inducible, considering the dependence on terms $S_{a,b}(x)$. Hence, as shown in the Supplementary Materials, the diffractive field and its intensity are inducible and follow

$$\begin{aligned} U_{N\times N}(x,y) = a^2 A_a(x) A_a(y) \left[\mathrm{Sinc}\left(a\frac{\pi}{z\lambda}x\right)\right]\left[\mathrm{Sinc}\left(a\frac{\pi}{z\lambda}y\right)\right] \times \ldots \\ \times\left\{\sum_{i=0}^{N-1}[S_{a,b}(x)]^i\right\}\left\{\sum_{i=0}^{N-1}[S_{a,b}(y)]^i\right\}, \end{aligned} \tag{2}$$

$$\begin{aligned} I_{N\times N}(x,y) = \frac{a^4\lambda^2}{4\pi^2 z^2}\mathrm{Sinc}^2\left(a\frac{\pi}{z\lambda}x\right)\mathrm{Sinc}^2\left(a\frac{\pi}{z\lambda}y\right) \times \ldots \\ \times\left|\sum_{i=0}^{N-1}[S_{a,b}(x)]^i\right|^2\left|\sum_{i=0}^{N-1}[S_{a,b}(y)]^i\right|^2. \end{aligned} \tag{3}$$

3. TIE as an Optical Test

The transport-of-intensity equation has been widely used in the literature since it constitutes a simple and accurate technique for optical testing in several examples as in flat surfaces [39], using Michelson interferometers [40] and for reconstructing the spatial parameters of a laser beam [41].

The transport-of-intensity equation (TIE) was deduced in 1983 by Teague [28], assuming an electromagnetic perturbation satisfying the wave equation [42]. Teague [28] built a hypothesis, where such a perturbation $u_z(\mathbf{r})$ satisfied the parabolic approximation of the wave equation

$$\left(i\frac{\partial}{\partial z} + \frac{\overrightarrow{\nabla_T}^2}{2k} + k\right)u_z(\mathbf{r}) = 0, \tag{4}$$

with $\mathbf{r} = (x,y)$ a vector, i denoting the imaginary unity, $k = 2\pi/\lambda$, and $\overrightarrow{\nabla_T} = (\partial/\partial x, \partial/\partial y)$ the nabla transversal operator. We assume the existence of an intensity term I satisfying $I_z(\mathbf{r}) = u_z(\mathbf{r}){u_z}^*(\mathbf{r})$ (with ${u_z}^*$ the conjugate complex of u_z), and a phase term $\phi_z(\mathbf{r})$, satisfying $u_z(\mathbf{r}) = \sqrt{I}e^{i\phi_z(\mathbf{r})}$. Hence, from Equation (4), we obtain the TIE by Teague [28] (Equation (5)):

$$\overrightarrow{\nabla_T}\left[I\left(\overrightarrow{\nabla_T}\phi_z\right)\right] = I\left(\overrightarrow{\nabla_T}^2\phi_z\right) + \left(\overrightarrow{\nabla_T}\phi_z\right)\cdot\left(\overrightarrow{\nabla_T}I\right) = -k\frac{\partial I}{\partial z}. \tag{5}$$

Thus, from Equation (5) and since the wavefront $W(x,y)$ follows $kW(x,y) = \phi_z(x,y)$, we obtain the elliptic equation coupled by the term $kW(x,y) = \phi_z(x,y)$. However, Ichikawa et al. [23] proposed a numerical form to decouple the differential equation, modifying the term $\partial I/\partial z$ with intensity measurements in two separate planes at a distance of 0.7 mm in $\Delta I/\Delta z = (I_2 - I_1)/(0.7\ \text{mm})$) (the distance choice comes from the instrumental limitations in the works by Ichiwaka et al. [23] and Arriaga et al. [26]). The latter reduces the TIE complexity to a second-order partial differential equation, from which we can solve $W(x, y)$ from the intensity measurements and with a suitable numerical method [26]. Moreover, the use of additional elements such as the Ronchi rulings (RR), inducing periodicity in the irradiance captures, allows the application of Fourier analysis both in its transform and series to filter several elements (noise, Fourier orders, and frequencies), making the technique by Ichikawa an optimal tool in surface sensing, using small shifts between different irradiance captures to obtain wavefront measurements. We focus on the latter for our proposal since the experimental RR noise issues are involved, having scarce control in the fringes period. In our proposal, we substitute the RR with spatial light modulators (SLMs), which, in addition to providing more control in the fringes period, allows the simulation of additional patterns, different from fringes.

4. Setups

4.1. Experimental

We implemented an experimental setup based in the experimental setups in Arriaga et al. [22,26], and Ichikawa et al. [23], using a 3.3 mW power He-Ne laser with $\lambda = 632$ nm, a $40\times$ microscope objective, a numerical aperture of 0.65, a pinhole with a diameter of 5 µm, a 2-inches diameter collimating lens (master), a focal distance of 50 mm, and a Ronchi ruling [43] (RR) with 50 lines per inch. Finally, we tested three 1-inches diameter lenses with focal distances of 150 mm, 100 mm, and 125 mm (L1, L2, and L3 respectively), previously tested and analyzed with ZYGO [27] and APEX (to validate the wavefronts obtained in our results). For the intensity captures, we use a Reflex (CCD) camera of 5184×3456 with a pixel size of 4.29 µm [22,23,26], which allows us to decrease the value of Δz (the CCD is placed on a mount with movement in z and shift controlled by a micrometric screw with a resolution of 0.1 µm, allowing to take intensity or irradiance captures in several z positions to obtain different intensities in Δz). The CCD is placed on a mount with XY movements, controlled by micrometric screws with a resolution of 10 nm. Roughly speaking, the aim of our proposal is to substitute the RR with an LCSLM, considering the experimental freedom and control that it offers, along with the solution methods, as we will address in the following.

4.2. Simulations

We simulate the TIE (as an optical test) [22,23], using our LCSLM (LCD) with the super-Gaussian (SG), instead of the Ronchi ruling (RR) [43], resembling the experimental setups in [17,20,44]. We replace the RR with fringes with SG profiles in the LCSLM (LCD). The size of the simulated LCD is 2 inches^2 with 1024×1024 pixels and a pixel size of 5 µm (the code is in the Github repository), despite that experimentally, it is a common practice to use a 1.45×1.09, inches^2 (36.9×27.6 mm^2; 1.8 inches^2) and a pixel size of 36 µm LCSLM after a simple polarizer of 2 inches in diameter (Figure 1). We illustrate the latter in Figure 1 and show the laser, collimating lens (master), LCD (HOLOEYE transmission SLM, LC 2012 Translucent Spatial Light Modulator) with a polarizer at a distance of 1 cm (placed after the LCD). The collimating lens is placed in a fixed position until a flat wavefront is obtained, irradiating the polarizer and the SLM in the same axis, and continuing with the propagation. The optical element under test is placed next to the polarizer, capturing its intensity with the CCD in the exit pupil.

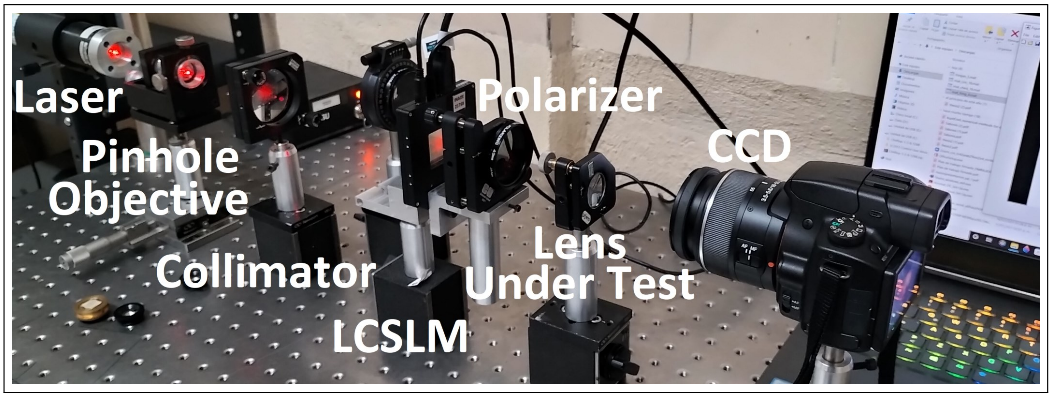

Figure 1. TIE simulation considering the laser illumination sources, pinhole objective, collimating lens (master), LCD (LC 2012 SLM, LCSLM) followed by a polarizer at 1 cm, the position of the object under test (L1, L2 and L3) and CCD. We replace the Ronchi ruling in the traditional TIE [23] with an LCSLM (along with a polarizer).

5. Early Results

5.1. Diffraction Patterns

Our results demonstrate that the LCD is an object resembling a fractal, in a periodic array with identical, equidistant apertures, as well as a diffractive object that is mathematically inducible. The tests in Equations (2) and (3), corresponding to detailed computations, are in the document Supplementary Materials. In such a document, we show that the simulated LCD produces a diffraction pattern, which is inducible [21] since the diffraction orders expansion follows the geometric series [36–38]. The latter can be experimentally tested by generating certain diffractive patterns [17,34,35,45,46]. We validate it, simulating the LCD with the code in Section IV in LCD_LCSLM_DiffPattern_SGR.m for 2×2, 3×3, 4×4 and 512×512 pixels, showing the intensity plots (Equation (3)) in Figure 2a–d, respectively, considering the 512×512-pixels LCD case (Section V), as the proof of the LCD as an inducible diffractive object (Supplementary Materials).

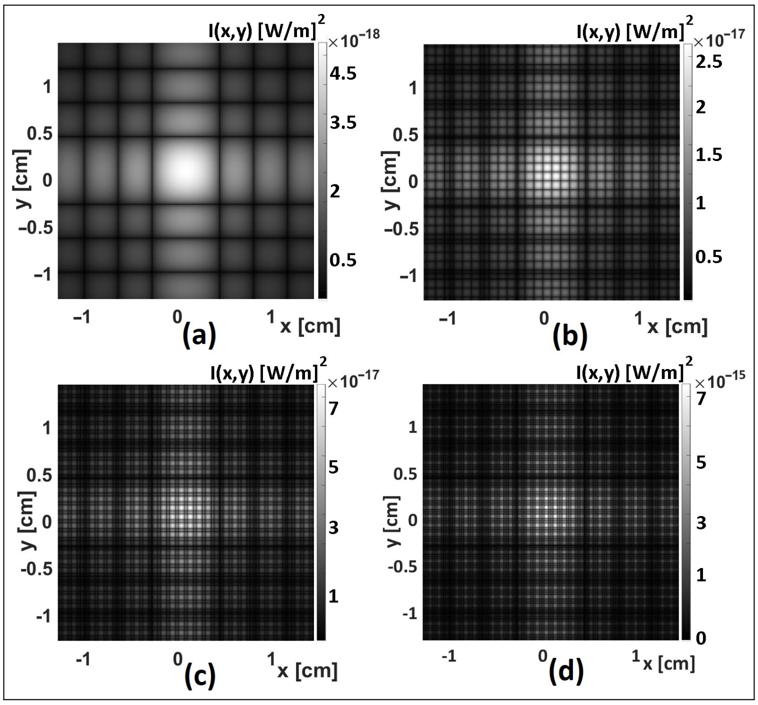

Figure 2. Intensity plots of the diffraction patterns for 2×2, 3×3, 4×4 and 512×512 pixels cases in (**a**), (**b**), (**c**), and (**d**) respectively. We include color bars of the intensity [W/m^2] on the right side of each panel.

5.2. Validating the LCSLM

In this step, we validate our simulation of the LCD and the rest of the SLM objects. Hence, according to Section 2, we use two test images or test charts to observe them using the LCD (Sections II and III in LCD_LCSLM_DiffPattern_SGR.m) in Figure 3a (Image obtained from "hwalworks" in https://www.hwalworks.com/The-Year-of-Resolution-Test-Chart, accessed on 24 December 2022) and Figure 3c (Image obtained from "ThorLabs" in https://www.thorlabs.com/newgrouppage9.cfm?objectgroup_id=4338, accessed on 24th December 2022). In Figure 3, we show the test charts in a 512×512 pixels LCD to observe the distributions using the LCD only. We do not show the 1024×1024 pixels LCD (used to obtain the final optimal results) since, due to the resolution of the images, there are no noticeable differences visually, resembling the absence of an LCD. The latter can be verified in the simulation code (previously mentioned) by modifying the variables AcPix $=$ 1024 (or 512) and TT $=$ 1200 (560), leading us to conclude that our LCD is capable of reproducing the desired patterns straightforwardly, providing reliable results. Subsequently, we show a zoom-in to the red squares placed on the right side of each chart in Figure 3b,d respectively.

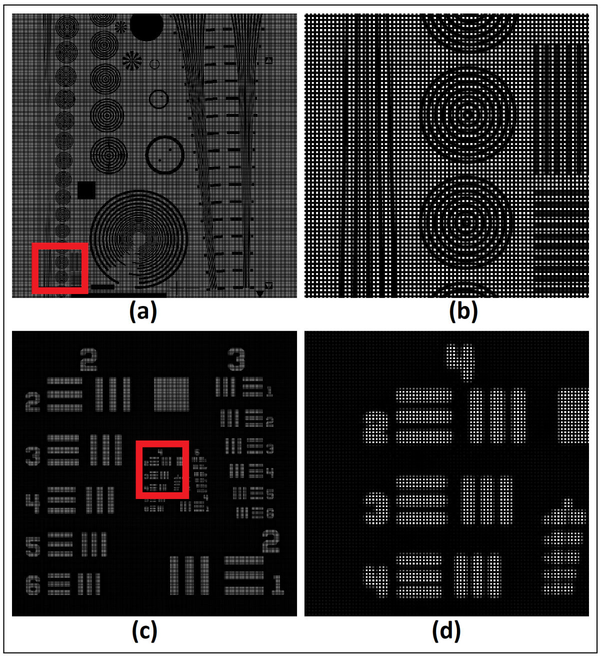

Figure 3. Visualization of two reference images or test charts in (**a**,**c**), observed using the 512×512-pixels simulated LCD. We perform a zoom-in to the red square in each image and show it in the right panels in (**b**,**d**), respectively.

5.3. Super-Gaussian Profiles

This result joins the previous tests of the simulated LCD, required to ensure that the desired patterns (super-Gaussians) are observed in the LCD (SLM) due to its periodicity and structure. We recall the inducible property of the diffraction patterns, inherited from the pixels' periodic layout, having both fractal geometry and series expansion features. The latter allows us to create the super-Gaussian profiles as a series, as we will see hereinafter. Hence, we recall in the first place that the Ronchi rulings (RRs) [43] are patterns constituted by parallel straight periodic fringes following a sinusoidal or cosine profile [47] that can be built in different materials, such as glass. However, some details appear in general during the printing procedure, introducing noise in the fringes, hindering the observation of the desired pattern (Figure 4c). With the aim of reducing this error in the RR in this work, we create a pattern resembling an RR with parallel periodic fringes, following, in this case, profiles similar to binary values (zeroes and ones) with super-Gaussian (SG) profiles according to the works developed in [48,49], described by the following expression:

$$SG_0 = I_G e^{-\left(\frac{|\mathbf{r}-\mathbf{r_0}|^2}{2\sigma^2}\right)^{\gamma}}, \tag{6}$$

with $2\sigma^2$ the relation between the SG spot size and width, and I_G the SG intensity centered in the vector $\mathbf{r_0}$. Hence, to build the SG pattern with parallel vertical fringes, we consider the vector $\mathbf{r} = \mathbf{x}$ and modify the SG center, replicating the process in order to obtain the complete desired fringes number. Such process is parameterized in terms of the width t in pixels, for each fringe and multiplied according to the LCD pixels number. The fringes can be either vertical or horizontal when considering the vector y instead of x. In our case, t has a value of 10.24 for each 1024×1024-matrix with 50 fringes since t is the ratio between twice the fringes number (transparent and opaque fringes) and the matrix pixel numbers (1024). Subsequently, we consider the value σ, regarding the fringe width, to account for the inter-fringes space, to ensure that the whole LCD is completely covered and all the fringes observed, as we illustrate in the repository (super-Gaussian fringes pattern in Section VI in LCD_LCSLM_DiffPattern_SGR.m). Hence, we build a periodic array with vertical parallel super-Gaussian (SG) fringes or super-Gaussian ruling (SGR). We describe the SGR construction observed in the LCD in the following expression:

$$SGR = \sum_{m=0}^{k-1} I_G e^{-\left(\frac{\mathbf{x}-[(2m+1)t+T]}{2\sigma^2}\right)^{\gamma}}, \tag{7}$$

with T the symmetry parameter of the LCD in pixels (for example, if we consider the center $T = -(N/2)$), k is the number of fringes, $t = N/(2k)$, with N the number of pixels and $\gamma = 80$. The choice of γ depends on the spatial modulator features (manufacturer, resolution, and the experimental conditions and the object under test). In our case, the SGR profiles were optimal for $\gamma = 74$. However, we recommend to replicate our results, and to fit other tests, $\gamma = 80$.

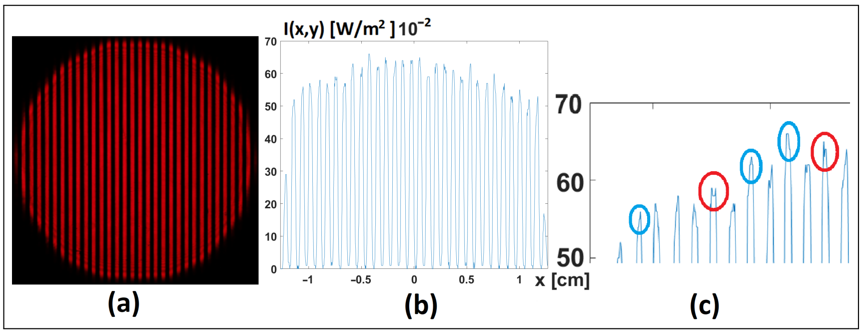

Figure 4. Experimental setups. In (**a**), intensity distribution cuts, considering a 25-lines per inch RR, in (**b**) longitudinal cut in (**a**), which we refer to as the intensity profile, and, in (**c**), zoom-in to (**b**).

6. Experimental Results

6.1. Fringes Error Reduction

As we mentioned in Sections 1 and 3, in order to test the optical elements applying the TIE, we require two intensity captures, which are obtained with the CCD [23,26] resulting in images similar to those in Figure 4a, (experimental intensity L1 lense) with the error mentioned in Section 5.3 (Figure 4c). In general, in this work, we measured the wavefronts from three different surfaces (L1, L2, L3), using three different procedures (ZYGO, TIE from Ichikawa et al. [23] and our proposal, validated and supported by the previously stressed arguments (our LCSLM proposal, see Figure 1), as we will mention hereinafter.

We bear in mind that originally, the TIE uses an RR [43] (Figure 4) [23,28]. For this reason, we propose a procedure analogous to the mentioned in [22,23,26], modified by a high-quality lens (master) and using an LCD (SLM) as we show in Figure 1. Subsequently, we can observe the intensity captures resulting from such modification in Figure 5, differing in their profiles since the fringes follow a super-Gaussian (SG) profile, despite looking similar to those in Figure 4a. After the SGR simulation (Figure 5a), such captures are analyzed in gray tones $[0, 255]$ to remove any other wavelength as well as chromatic errors [47] (Figure 5d). In order to validate the SG profiles, we perform transversal cuts to the profiles observed in the LCD with the SGR (Figure 5c). The error observed in the fringes using the RR in Figure 4c is no longer observed in Figure 5e. In order to accomplish our goal of applying the LCSLM with SGR in the TIE, we remove this error in the fringes, which subsequently propagates up to the resulting wavefront [26,47].

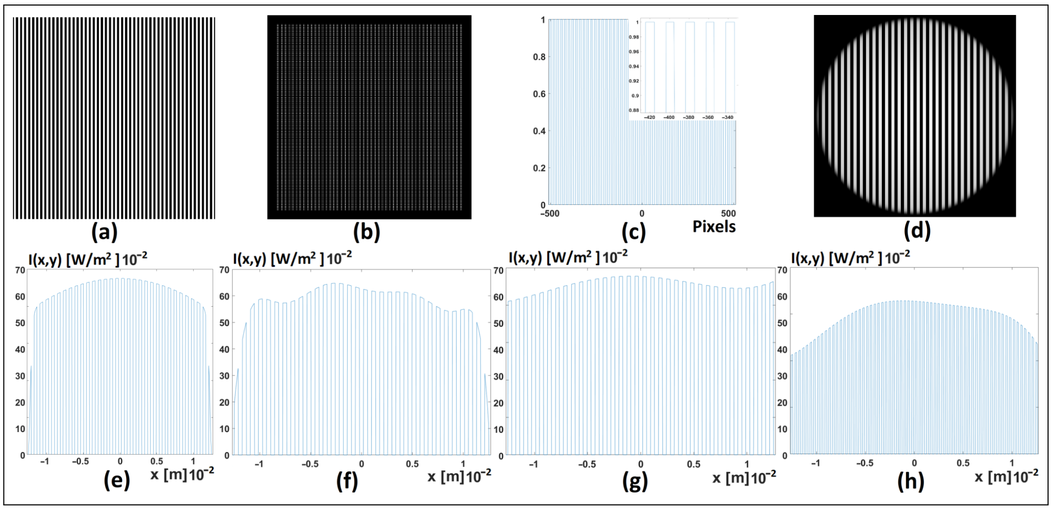

Figure 5. In (**a**) 50-fringes per inch SGR. In (**b**), the pattern in (**a**) is observed through the LCD, simulating the screen and the LCSLM width. In (**c**), we show the profile in (**d**). In (**b**), the 512 × 512-pixels LCD for illustrative purposes. In (**d**), we show the simulation of Figure 4a, considering the L1 pupil. In (**e**), the ideal profile of (**d**), whereas in (**f**), the simulations of the aberrations and deformations in the experimental intensity in Figure 4a and we show the corresponding profile. In (**f**,**g**,**h**), we show the intensities profile of L1, L2 and L3 (respectively), considering the LCSLM simulating the SGR.

We emphasize that our proposal to implement the SGR modelled in an LCD (LCSLM) can be used in several cases as an alternative to reduce the noise or error (Figure 4c). For instance, in Figure 4c, we show the errors in the RR implementation, in the conventional TIE in red and blue circles, with the blue ones showing the errors changing the peak location, which should be centered, whereas the red circles have several peaks in given fringes, where a single peak is expected. Both errors represent deformations in the centroid position and, its interpretation, affecting the aberrations calculations [47]. Moreover, in Figure 4a,b, we notice that the fringe widths are not symmetrical, which could be due to the RR material quality and certain unwanted rotation. Our proposal to implement the LCD or LCSLM is suitable to correct some of the previously mentioned errors, such as the chromatic ones, diffractive and refractive errors, and several unwanted reflections [33–35,47]. The peak bias errors can be removed due to the SGR uniformity, and the continuity of the transmittance distribution super-Gaussian (SG) functions [48,49].

6.2. Intensity Captures

Since the LCD efficiency was validated, we can simulate a pupil function, considering a uniform intensity distribution passing through the SGR in the LCD (Figure 5d), master and the surface under test (L1, L2 or L3, Figure 1). In Figure 5f–h, we show the intensity distributions for the surfaces under test L1, L2, and L3 (respectively), with the SGR patterns in the SLM (we show one capture or intensity distribution $I(x, y)$ only since the following at 0.5 µm [26] does not display visually significant differences). Unlike the ideal intensity profile (Figure 5e) the experimental profiles (even in the spheric lenses case of the elements under test (L1, L2, and L3) differ significantly from the ideal one (Figure 5f–h) due to their aberrations. Subsequently, we consider all the peaks to build a curve joining all the points, resembling a point cloud inside a curve [22,26], by performing a polynomial fit. The fitting curve contains the experimental profile of the intensity distribution, which allows us to fit the 3D profile of the intensity distribution, considering its propagation, the exit pupil of the optical system, edge errors [47] and the deformations due to the system itself (Figure 5f–h). From the simulations in Figure 5d,f, we show a technique enabling us to control an LCSLM in optical tests (TIE [23,26,28]), offering the possibility to modify or implement numerical patterns and using unknown patterns in the LCD since we can numerically control some elements, commonly containing errors, by removing them from the results, and experimentally, we can remove chromatic and polarization errors.

Given that the wavefront W is obtained from the TIE solution (Equation (5)), manipulating the intensity captures $I(x,y)$ as described in the previous paragraph, we obtain a periodic pattern SGR (in the LCD), which minimizes the errors. Subsequently, in order to optimize our proposal, we require an optimal interpretation of the intensity captures $I(x,y)$ with the aim of obtaining $W(x,y)$. Hence, we apply the point cloud method to each $I(x,y)$ as a 2D surface. Thus, a certain common numerical error can be reduced using the point cloud from transversal cuts in $I(x,y)$, considering the relative maxima in each cut [26]. For the purposes of this work, we use 21 transversal cuts (considering 50 SGR fringes) for each $I(x,y)$ per element under test (L1, L2, and L3), shown in Figure 6a,c,e for L1, L2 and L3, respectively. Finally, we perform a polynomial fitting with less dispersion to the point cloud, and we show it in Figure 6b,d,f, associated to the Figure 6a,c,e, respectively.

6.3. Obtaining the Wavefront

We obtain the wavefront by numerically solving the TIE (Equation (5)). To this aim, we require at least two intensity captures (ΔI) with a separation between the capture planes Δz (in our work $\Delta z = 0.5\,\mu\text{m}$, which comes from the work by Arriaga et al., 2020 [50], three orders of magnitude lower than the value in Sections 3 and 4; this value allows us to reduce the wavefront propagation errors, as well as some edge defects in the surfaces under test [47,50]), and satisfying $\frac{\partial I}{\partial z} \approx \frac{\Delta I}{\Delta z}$ in the right side of Equation (5) to decouple the elliptical differential equation. Considering this along with the results in Figure 6, we can apply several numerical methods to recover the wavefront $W(x,y)$ from Equation (5), such as finite element, finite differences, etc. [51,52]. In our case, we use the finite differences method [53] to obtain $W(x,y)$ as a 2D surface from the numerical solution [22,26]. Therefore, we consider two fits per point cloud per $I(x,y)$ for ΔI to obtain $\Delta I/\Delta z$, and finally, the data in Equation (5) to numerically solve $W(x,y)$ with the finite differences method [51,53], as mentioned in Arriaga et al. [22,26]. As a direct consequence of the numerical solution from the TIE, we obtain the wavefronts $W(x,y)$ in rectangular coordinates, which need to be transformed into polar coordinates in order to be analyzed in terms of the Zernike aberrations polynomials [24–26]. Subsequently, from $W(\rho,\theta)$, we obtain the aberration coefficients up to the 12-th degree, applying the least-square multi-linear regression method [54] of the data using the following expression:

$$W(\rho,\theta) = \sum_{i=0}^{M}\sum_{j=-i}^{i} b_{i,j} Z_{i,j}(\rho,\theta), \quad (8)$$

with $Z_{i,j}(\rho,\theta)$ the Zernike polynomials [24–26], M the polynomial degree expansion and $W(\rho,\theta)$. By virtue of theorems in statistics and probability theory, regarding the central limit theorem, it is straightforward to conclude that for larger M values, the dispersion and error will be minimal. Hence, we perform a $M = 30$-degree fit (obtaining 496 Zernike coefficients $b_{i,j}$ per test). Our proposal is focused on modifying the TIE as an optical test using the SLM (recalling that an RR is used in the TIE). In order to validate our proposal, we compare the wavefront $W(\rho,\theta)$ with those obtained by well-known tools, such as ZYGO [27] and APEX. ZYGO is capable of providing the interferogram, whereas APEX analyzes it in order to obtain the Zernike aberrations polynomial [24–26]. We call that interferogram the ZYGO/APEX. Since the order of our fit is high [26], the coefficients obtained by APEX are less in quantity than those obtained by our fit. Hence, in Figure 7, we show two columns of images of $W(\rho,\theta)$. In the left panels we show $W(\rho,\theta)$ of our proposal for the lenses L1, L2 and L3 (Figure 7a,c,e respectively). On the other hand, in the right panels, we show $W(\rho,\theta)$ obtained by ZYGO/APEX for L1, L2 and L3 (Figure 7b,d,f respectively). After a simple visual comparison, we observe that the obtained wavefronts are very similar, giving reliability to the results obtained with our proposal. Subsequently, we mention that some aberration coefficients up to 12th degree are obtained with ZYGO/APEX, among which are the piston, tilt, tip, coma, astigmatism, trefoil, quadrafoil and spherical. However, these are not all the coefficients. On the other hand, our proposal allows us to obtain up to 30th degree, and hence, it is possible to obtain all the coefficients. Furthermore, higher degrees could be fitted depending on the available computing power [22,26].

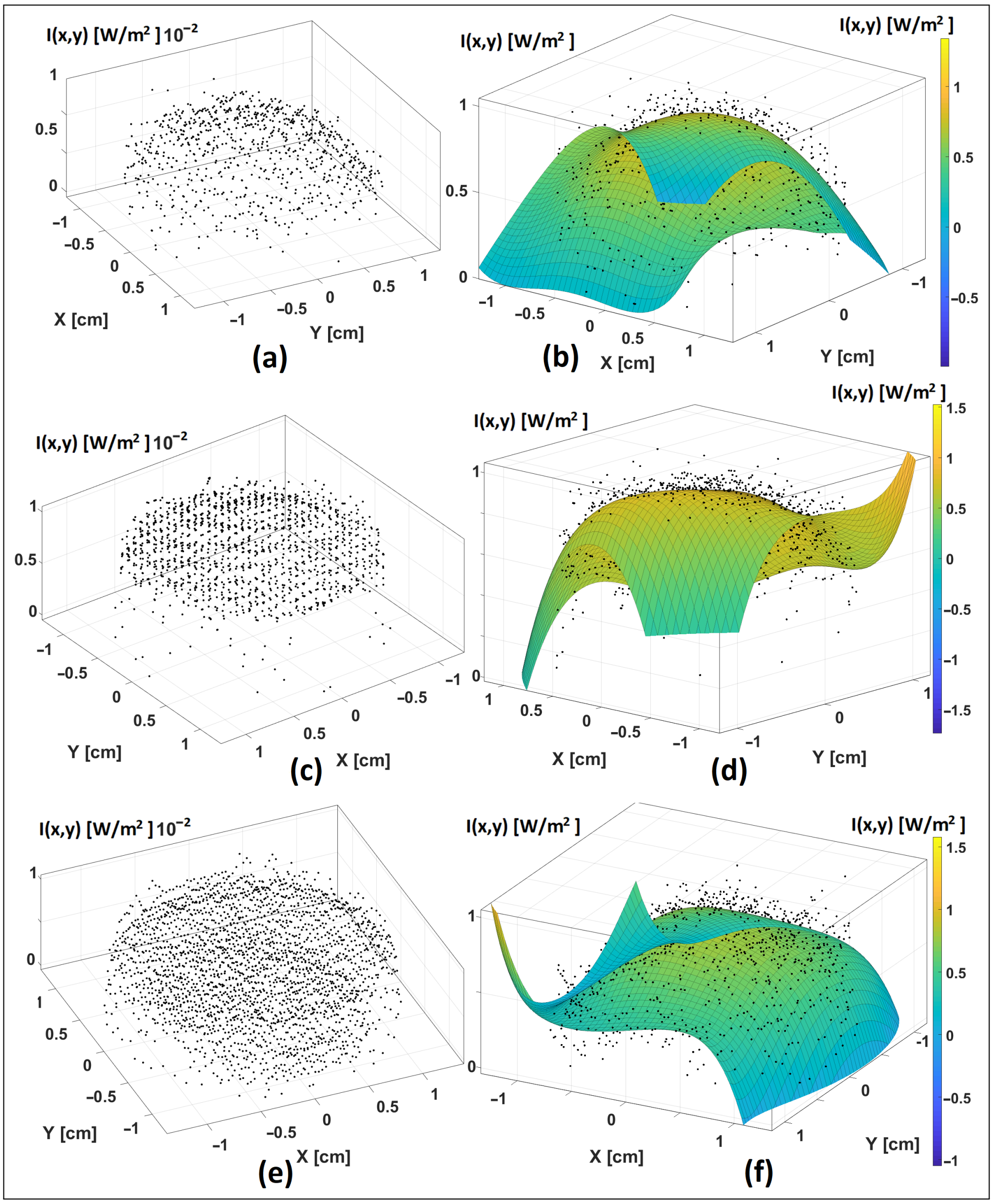

Figure 6. In (**a**,**c**,**e**) we show relative maxima for 21 transversal cuts, considering only the 50 fringes in the SGR in the simulated LCD (point cloud) for L1, L2, and L3, respectively. In (**b**,**d**,**f**), the polynomial curve fitting the point cloud in (**a**,**c**,**e**), respectively.

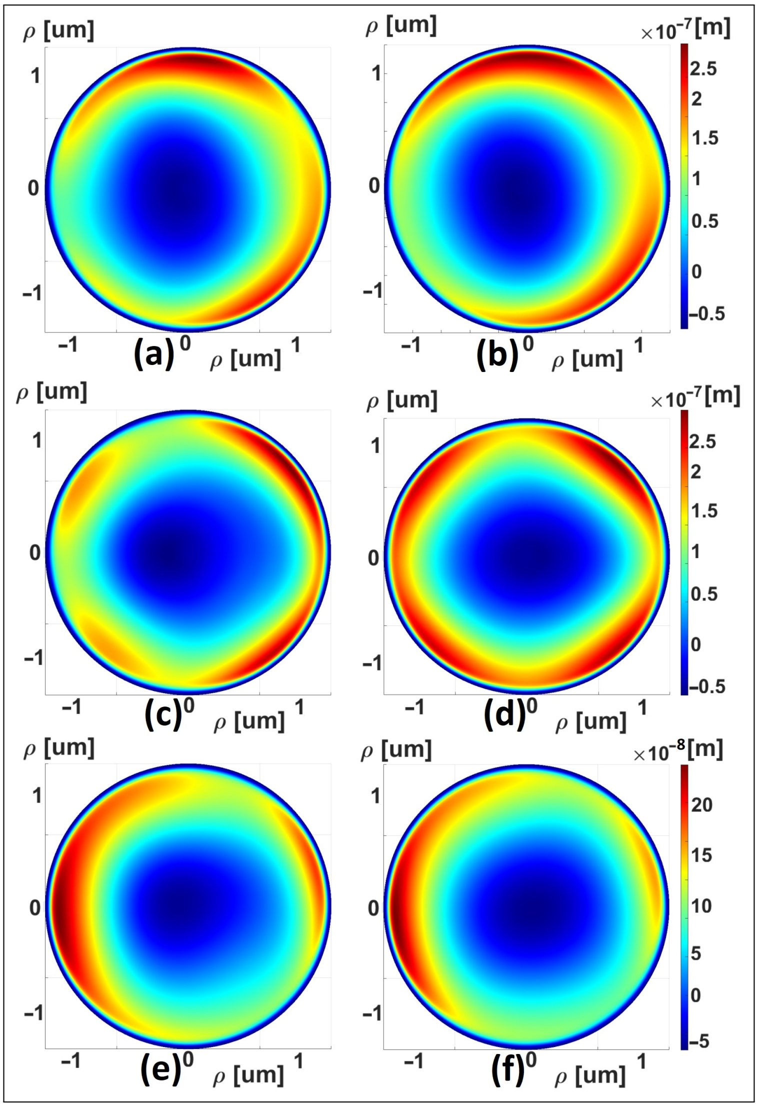

Figure 7. Obtained wavefronts $W(\rho,\theta)$ by a $M = 30$-degree fitting from Equation (8) in (**a**,**c**,**e**) of the SGR in the simulated LCD, from experimental data of L1, L2, and L3 respectively. In (**b**,**d**,**f**), we show the fits to the software and hardware data ZYGO/APEX of the same lenses L1, L2, and L3, respectively.

We perform in Equation (8) a $M = 30$-degree fit to the APEX results (in order to compare our experimental results coefficient by coefficient) according to Equation (8). We include such coefficients in the repository (CoeZernExpL*i*_coeff.mat for the SGR in the simulated LCD and CoeZernZYGOL*i*_coeff.mat for the APEX results fit, for each L*i* with $i = 1,2,3$ respectively) following the ANSI ordering protocols. Thus, for the fits performed to the ZYGO/APEX results, we obtained in average a dispersion value of 1 nm and an error of 0.01% between the fitting curves and the results by ZYGO/APEX. The fits to the simulated results by the SGR in the LCD are 2.988 nm with an RMS of 0.09631 for L1, 5.562 nm with an RMS of 0.08097 for L2, and 2.041 nm with an RMS of 0.0101 for L3. We bear in mind that for a ruling with higher frequency, the results are slightly optimized, which can be visually validated in the wavefronts in Figure 7.

Finally, we recall that our proposal is a direct modification of the conventional TIE by Ichikawa et al. [23] also studied by Arriaga et al. [22,26]. In our proposal, we use the LCSLM with SGR patterns instead of the RR (conventional TIE). Hence, we can consider the conventional TIE to compare our results. Thus, we also analyze the lenses L1, L2, and L3 with the conventional TIE (Sections 4 and 4.1), and compare the $W(\rho,\theta)$ results obtained using three techniques: our proposal, the conventional TIE and ZYGO/APEX. We show the data from the comparison in Table 1, where we perform a simple comparison between the main aberration coefficients, following the ANSI ordering protocols.

Table 1. We show the main aberration coefficients (following the ANSI ordering protocols) corresponding to L1, L2, and L3, obtained experimentally, applying the TIE with the RR, simulating the SGR in the LCD and the data obtained by ZYGO/APEX.

L1 [m] $\times 10^{-8}$					
ANSI	Coeff	Aberration	Exp RR	SGR in LCD	ZYGO/APEX
1	$b_{0,0}$	piston	11.5223	12.4140	12.1610
5	$b_{2,0}$	defocus	6.9981	7.3471	7.3831
4	$b_{-2,2}$	Astig 45°	−1.4970	−1.5073	−1.5587
6	$b_{2,2}$	Astig 0°	−1.9338	−2.0570	−2.0855
8	$b_{3,-1}$	coma x	−0.5006	−0.5890	−0.4807
9	$b_{3,1}$	coma y	−1.6599	−1.7658	−1.8214
13	$b_{4,0}$	Spherical	−8.9067	−8.3279	−8.2557
L2 [m] $\times 10^{-8}$					
ANSI	Coeff	Aberration	Exp RR	SGR in LCD	ZYGO/APEX
1	$b_{0,0}$	piston	12.9901	13.9450	13.2360
5	$b_{2,0}$	defocus	8.2316	8.8043	9.0063
4	$b_{-2,2}$	Astig 45°	0.4003	0.3721	0.1800
6	$b_{2,2}$	Astig 0°	−0.4733	−0.4895	−0.5259
8	$b_{3,-1}$	coma x	−0.1723	−0.1670	−0.1506
9	$b_{3,1}$	coma y	1.9801	2.5862	0.5937
13	$b_{4,0}$	Spheric	−8.0072	−8.8874	−8.4999
L3 [m] $\times 10^{-8}$					
ANSI	Coeff	Aberration	Exp RR	SGR in LCD	ZYGO/APEX
1	$b_{0,0}$	piston	9.3109	9.5123	9.2009
5	$b_{2,0}$	defocus	5.7501	5.5605	5.6785
4	$b_{-2,2}$	Astig 45°	1.9988	3.0229	0.2762
6	$b_{2,2}$	Astig 0°	2.0089	2.1026	2.1489
8	$b_{3,-1}$	coma x	−0.5006	−0.4412	−0.2752
9	$b_{3,1}$	coma y	0.4591	0.4653	0.3170
13	$b_{4,0}$	Spherical	−6.7001	−6.6191	−6.4783

In the first place, we bear in mind that a more exhaustive and complete comparison can be performed with the most relevant coefficients in our proposal and ZYGO/APEX (CoeZernExpL1_coeff.mat and CoeZernZYGOL1_coeff.mat). In Table 1, we observe that some coefficients are similar, with an error close to 0.001%, as in the case of piston, spherical, and astigmatism (0°) for L1 and L3. However, in the L2 case, the error increases up to 0.1%, and 1%, as expected due to its RMS close to 0.1, which differs from the values corresponding to the observed profile in Figure 5g since there are no significant deformations. However, we recall the lack of a bulk of coefficients for fitting. However, from the RMS values associated with L1, L2, and L3 (0.09631, 0.08097 and 0.0101, respectively), we can verify that the most aberrated lens is L1, followed by L2, and L3 is the less aberrated lens or with a profile closer to a spherical one (Figure 5). Another error produced by considering the primary aberrations only (column 1 in Table 1) occurs when considering the dispersion value only between the data in Table 1 since the largest value is reached by L2 with 0.6%, which is not the case. Moreover, our proposal seems to have larger dispersion than the conventional TIE. However, it is only an error due to the lack of coefficients since in general terms our proposal reduces by up to 1%, the error margin regarding the conventional TIE due to errors shown in Figure 4, associated to the RR.

7. Conclusions

In this work, we show the TIE [28] as an optical test modified with the experimental application of an LCSLM (simulating and LCD) with SG patterns, optimizing the results. The objectives were the LCD simulation and its validation, which lead us to show that the diffraction pattern is inducible when the LCD has periodic patterns. Hence, we highlight several contributions of our work: in the first place, the LCD as a diffractive inducible object, which provides the SLM with certain geometric and fractal elements in several areas; in the patterns simulation with more complex structure as the structured beams used in the analysis of medical images and biological samples; and in optical trapping in the use of vortex lenses, both with the aim of retrieving the phase and identifying errors and anomalies [55]. In general, we show an option to substitute the RR in glass to reduce errors if the experimental setup allows it when considering the sizes of the SLM and polarizers. Subsequently, we show that the periodical equidistant fringes representing the Ronchi ruling [43] can be substituted by patterns with super-Gaussian (SG) profiles. We are aware that these patterns have been widely used in the literature in other applications. However, we contribute with a different application of such patterns to remove errors in the fringes profiles. Moreover, we bear in mind that the SGR in Equation (7) inherits as well the LCSLM geometrical properties by being simulated on it. We are delving into several inducible applications of the SGR as an algebraically convergent series and generating base of other patterns. Moreover, we are exploring applications beyond surface testing, for example in biophotonics. Finally, our main objective was obtaining the wavefront from experimental data, which included all the previous objectives, in addition to the simulation of the experimental intensity profiles using the SGR in the LCD. We acknowledge the accomplishment of this objective by observing the percentage errors and the obtained RMS, considering the data in the repository as well as the aberration coefficients in Table 1. These results depend mostly on the point cloud method [26], which is a widely used method in electronics and computer science in data processing, in addition to an accurate numeric interpolation method. We obtain the intensities with this method. It can be applied also to the wavefront. However, due to the execution times, we did not perform such estimation in this work. The latter represents also a numerical contribution to the information processing since it allows us to obtain reliefs from the maxima. However, in the Matlab ® case, an image processing and fit data Toolbox is required for its application. The description laid out in this work can be used to build a simple algorithm and fitting that can be implemented with any suitable known function.

Supplementary Materials: The following supporting information can be downloaded at: https://www.mdpi.com/article/10.3390/photonics10010039/s1.

Author Contributions: Conceptualization, J.A.-H., B.C.-O., J.O.-O. and M.M.-C.; methodology, J.A.-H., B.C.-O., J.O.-O. and M.M.-C.; software, J.A.-H. and B.C.-O.; validation, J.A.-H., B.C.-O., J.O.-O., M.M.-C., Y.M.-L. and L.C.-R.; formal analysis, J.A.-H., B.C.-O., J.O.-O. and M.M.-C.; investigation, J.A.-H., B.C.-O., J.O.-O., M.M.-C., Y.M.-L. and L.C.-R.; resources, J.O.-O., M.M.-C., Y.M.-L. and L.C.-R.; data curation, Y.M.-L. and L.C.-R.; writing—original draft preparation, J.A.-H. and B.C.-O.; writing—review and editing, J.A.-H., B.C.-O., J.O.-O., M.M.-C., Y.M.-L. and L.C.-R.; visualization, J.O.-O., M.M.-C., Y.M.-L. and L.C.-R.; supervision, J.A.-H. and B.C.-O. All authors have read and agreed to the published version of the manuscript.

Funding: This research received no external funding.

Institutional Review Board Statement: Not applicable.

Informed Consent Statement: Not applicable.

Data Availability Statement: Publicly available datasets were analyzed in this study. This data can be found here: https://github.com/umbramortem/SG_profile_LCLSM_inductible_diffractive.

Acknowledgments: The authors want to thank the Benemerita Universidad Autonoma de Puebla (BUAP) for the support given during this research work. We also thank CONACYT (Consejo Nacional de Ciencia y Tecnologia, México).

Conflicts of Interest: The authors declare no conflict of interest.

References

1. Hornbeck, L.J. Digital light processing for high-brightness high-resolution applications. In Proceedings of the Projection Displays III, Electronic Imaging '97, San Jose, CA, USA, 8 May 1997; Volume 3013, pp. 27–40. [CrossRef]
2. Zhang, T.; Kho, A.M.; Srinivasan, V.J. Improving visible light OCT of the human retina with rapid spectral shaping and axial tracking. *Biomed. Opt. Express* **2019**, *6*, 2918–2931. [CrossRef] [PubMed]
3. Matsumoto, N.; Inoue, T.; Matsumoto, A.; Okazaki, S. Correction of depth-induced spherical aberration for deep observation using two-photon excitation fluorescence microscopy with spatial light modulator. *Biomed. Opt. Express* **2015**, *6*, 2575–2587. [CrossRef] [PubMed]
4. Khan, S.; Jesacher, A.; Nussbaumer, W.; Bernet, S.; Ritsch-Marte, M. Quantitative analysis of shape and volume changes in activated thrombocytes in real time by single-shot spatial light modulator-based differential interference contrast imaging. *J. Biophotonics* **2011**, *4*, 600–609. [CrossRef] [PubMed]
5. Ibrahim, D.G.A.; Bakr, R.H. Viewing label-free white blood cells using phase-only spatial light modulator. In *Frontiers in Optics + Laser Science*; Mazzali, C., Poon, T.(T.-C.), Averitt, R., Kaindl, R., Eds.; Technical Digest Series, Paper JW7A.123; Optica Publishing Group: Washington DC, WA, USA, 2021. [CrossRef]
6. Ibrahim, D.G.A.; Abdelazeem, R.M. Quantitative Phase Imaging by Automatic Phase Shifting Generated by Phase-only Spatial Light Modulator. In *Frontiers in Optics + Laser Science*; Mazzali, C., Poon, T.(T.-C.), Averitt, R., Kaindl, R., Eds.; Technical Digest Series Paper JTh5A.104; Optica Publishing Group: Washington DC, WA, USA, 2021. [CrossRef]
7. Wen, S.; Bhaskar, A.; Zhang, H. Scanning digital lithography providing high speed large area patterning with diffraction limited sub-micron resolution. *J. Micromech. Microeng.* **2018**, *28*, 075011. [CrossRef]
8. Kagalwala, K.H.; Di-Giuseppe, G.; Abouraddy, A.F.; Saleh, B. Single-photon three-qubit quantum logic using spatial light modulators. *Nat. Comm.* **2017**, *8*, 739. [CrossRef]
9. Storrs, M.; Mehrl, D.J.; Walkup, J.F.; Krile, T.F. Volterra series modeling of spatial light modulators. *Appl. Opt.* **1998**, *37*, 7472–7481. [CrossRef]
10. Slinger, C.; Cameron, C.; Stanley, M. Computer-generated holography as a generic display technology. *Computer* **2005**, *38*, 46–53. [CrossRef]
11. Chandra, A.D.; Karmakar, M.; Nandy, D.; Banerjee, A. Adaptive hyperspectral imaging using structured illumination in a spatial light modulator-based interferometer. *Opt. Express* **2022**, *30*, 19930–19943. [CrossRef]
12. Hara, T. A liquid crystal spatial light phase modulator and its applications. In *Information Optics and Photonics Technology, Proceedings of the Photonics Asia, Beijing, China, 11 January 2005*; SPIE: Bellingham, WA, USA, 2004; Volume 5642, pp. 78–89. [CrossRef]
13. Chandra, A.D.; Banerjee, A. Rapid phase calibration of a spatial light modulator using novel phase masks and optimization of its efficiency using an iterative algorithm. *J. Modern Opt.* **2020**, *67*, 628–637. [CrossRef]
14. Davis, J.A.; Tsai, P.S.; Cottrell, D.M.; Sonehara, T.; Amako, J.; Santillan, A. Transmission variations in liquid crystal spatial light modulators caused by interference and diffraction effects. *Opt. Eng.* **1999**, *38*, 1051–1057. [CrossRef]
15. Pérez-Cabré, E.; Millán-Sagrario, M. Liquid Crystal Spatial Light Modulator with Optimized Phase Modulation Ranges to Display Multiorder Diffractive Elements. *App. Sci.* **2019**, *9*, 2592. [CrossRef]
16. Katz, B.; Rosen, J.; Kelner, R.; Brooker, G. Enhanced resolution and throughput of Fresnel incoherent correlation holography (FINCH) using dual diffractive lenses on a spatial light modulator (SLM). *Opt. Express* **2012**, *20*, 9109–9121. [CrossRef] [PubMed]
17. Agour, M.; Kolenovic, E.; Falldorf, C.; von-Kopylow, C. Suppression of higher diffraction orders and intensity improvement of optically reconstructed holograms from a spatial light modulator. *J. Opt.* **2009**, *11*, 105405. [CrossRef]
18. Frantz, M. A Fractal Made of Golden Sets. *Math. Mag.* **2009**, *82*, 243–254. Available online: https://www.jstor.org/stable/27765915 (accessed on 24 December 2022). [CrossRef]
19. Horváth, P.; Šmíd, P.; Vašková, I.; Hrabovský, M. Koch fractals in physical optics and their Fraunhofer diffraction patterns. *Optik* **2010**, *121*, 206–213. [CrossRef]
20. Wang, J.; Zhang, W.; Cui, Y.; Teng, S. Fresnel diffraction of fractal grating and self-imaging effect. *Appl. Opt.* **2014**, *53*, 2105–2111. [CrossRef]
21. Henkin, L. On Mathematical Induction. *Am. Math. Mon.* **1960**, *67*, 323–338. [CrossRef]
22. Arriaga-Hernández, J.A.; Granados-Agustín, F.; Cornejo-Rodríguez, A. Measurement of three-dimensional wavefronts using the Ichikawa-Lohmann-Takeda solution to the irradiance transport equation. *Appl. Opt.* **2018**, *57*, 4316–4321. [CrossRef]
23. Ichikawa, K.; Lohmann, A.W.; Takeda, M. Phase retrieval based on the irradiance transport equation and the Fourier transform method: Experiments. *Appl. Opt.* **1988**, *27*, 3433–3436. [CrossRef]
24. Vasudevan, L.; Fleck, A. Zernike polynomials: A guide. *J. Mod. Opt.* **2011**, *58*, 545–561. [CrossRef]

25. von-Zernike, F. Beugungstheorie des schneidenver-fahrens und seiner verbesserten form, der phasenkontrastmethode. *Physica* **1934**, *1*, 689–704. [CrossRef]
26. Arriaga, J.A.; Cuevas, B.T.; Oliveros, J.J.; Jaramillo, A.; Morín, M. Irradiance transport equation applied to propagation of wavefront obtained by the Bi-Ronchi test using point cloud. *J. Phys. Commun.* **2021**, *5*, 055019. [CrossRef]
27. Forman, P.F. Digital light processing for high-brightness high-resolution applications. In Proceedings of the 23rd Annual Technical Symposium, San Diego, CA, USA, 25 December 1979; Volume 0192, pp. 41–49. [CrossRef]
28. Teague, M.R. Deterministic phase retrieval: A Green's function solution. *J. Opt. Soc. Am.* **1983**, *73*, 1434–1441. [CrossRef]
29. Mohamed, N. *Digital Filters Design for Signal and Image*; Wiley-ISTE: Newport Beach, CA, USA, 2008. [CrossRef]
30. Pratt, W.K. *Digital Image Processing*; John Wiley & Sons: Los Altos, CA, USA, 2002. [CrossRef]
31. Vetterli, M.; Kovačević, J.; Goyal, V.K. *Foundations of Signal Processing*; Cambridge University Press: Cambridge, UK, 2014. [CrossRef]
32. Arendt, W.; Schleich, W.P. *Mathematical Analysis of Evolution, Information, and Complexity*; Wiley-VCH Verlag GmbH & Co. KGaA: Weinheim, Germany, 2009. [CrossRef]
33. Mandel, L.; Wolf, E. *Optical Coherence and Quantum Optics*; Cambridge University Press: Rochester, NY, USA, 1995. [CrossRef]
34. Born, M.; Wolf, E. *Principles of Optics: Electromagnetic Theory of Propagation, Interference and Diffraction of Light*; Cambridge University Press: Cambridge, UK, 2000. [CrossRef]
35. Goodman, J.W. *Introduction to Fourier Optics*; E W. H. Freeman Press: San Francisco, CA, USA, 2005. [CrossRef]
36. Roe, E.D. Note on Integral and Integro-Geometric Series. *Ann. Math.* **1896**, *11*, 184–194. [CrossRef]
37. Arfken, G.B.; Weber, H.J.; Harris, F. *Mathematical Methods for Physicists*; Elsevier Academic Press: London, UK, 2012. [CrossRef]
38. Hirst, K. *Numbers, Sequences and Series*; Elsevier Academic Press: Southampton, UK, 1994.
39. Dorrer, C.; Zuegel, J.D. Optical testing using the transport-of-intensity equation. *Opt. Express* **2007**, *15*, 7165–7175. [CrossRef]
40. Gupta, A.K.; Mahendra, R.; Nishcal, K.N. Single-shot phase imaging based on transport of intensity equation. *Opt. Comm.* **2020**, *477*, 126347. [CrossRef]
41. Kovalev, M.; Gritsenko, I.; Stsepuro, N.; Nosov, P.; Krasin, G.; Kudryashov, S. Reconstructing the Spatial Parameters of a Laser Beam Using the Transport-of-Intensity Equation. *Sensors* **2022**, *5*, 1765. [CrossRef]
42. Verdeyen, J.T. *Laser Electronics*; Prentice Hall Press: Urbana, IL, USA, 1995.
43. Ronchi, V. Due nuovi metodi per lo studio delle superficie e dei sistemi ottici. In *Annali della Scuola Normale Superiore di Pisa–Classe di Scienze;* Springer Nature: Berlin/Heidelberg, Germany, 1927; Volume 69, pp. 69–71. [CrossRef]
44. Bergeron, A.; Gauvin, J.; Gagnon, F.; Gingras, D.; Arsenault, H.H.; Doucet, M. Phase calibration and applications of a liquid-crystal spatial light modulator. *Appl. Opt.* **1995**, *34*, 5133–5139. [CrossRef]
45. Shetty, P.P.; Bingi, J. Demonstration of synergic Fresnel and Fraunhofer diffraction for application to micrograting fabrication. *Opt. Laser Technol.* **2020**, *130*, 106340. [CrossRef]
46. Zhou, J.; Cao, Z.; Xie, H.; Xu, L. Digital micro-mirror device-based detector for particle-sizing instruments via Fraunhofer diffraction. *Appl. Opt.* **2015**, *54*, 5842–5849. [CrossRef]
47. Malacara, D. *Optical Shop Testing*; John Wiley & Sons Inc.: Hoboken, NJ, USA, 2007. [CrossRef]
48. Bissell, J.J.; Ridgers, C.P.; Kingham, R.J. Super-Gaussian transport theory and the field-generating thermal instability in laser–plasmas. *New J. Phys.* **2013**, *15*, 025017. [CrossRef]
49. De-Silvestri, S.; Laporta, P.; Magni, V.; Svelto, O. Solid-state laser unstable resonators with tapered reflectivity mirrors: The super-Gaussian approach. *J. Quantum Electron.* **1988**, *24*, 1172–1177. [CrossRef]
50. Arriaga, J.A.; Cuevas, B.T.; Oliveros, J.J.; Jaramillo, A.; Morín, M. Filter construction using Ronchi masks and Legendre polynomials to analyze the noise in aberrations by applying the irradiance transport equation. *Appl. Opt.* **2020**, *59*, 3851–3860. [CrossRef] [PubMed]
51. Glowinski, R.; Neittaanmäki, P. Partial Differential Equations: Modelling and Numerical Simulation. In *Computational Methods in Applied Sciences*; Springer: Dordrecht, The Netherlands, 2008. [CrossRef]
52. Glowinski, R. Finite element methods for incompressible viscous flow. In *Handbook of Numerical Analysis*; Elsevier: Amsterdam, The Netherlands, 2003; Volume 9, pp. 3–1176. [CrossRef]
53. Yin, P.; Liandrat, J.; Shen, W. A comparison of the finite difference and multiresolution method for the elliptic equations with Dirichlet boundary conditions on irregular domains. *J. Comput. Phys.* **2021**, *343*, 110207. [CrossRef]
54. Birkes, D.; Dodge, D. *Alternative Methods of Regression*; John Wiley & Sons: New York, NY, USA, 1993.
55. Arriaga, J.A.; Cuevas, B.T.; Oliveros, J.J.; Jaramillo, A.; Morín, M. Geometric aberrations in the 3D profile of microparticles observed in optical trapping using 2D Legendre polynomials. *Optik* **2022**, *249*, 168123. [CrossRef]